Chapter 18

INSTABILITY OF ISOCHRONOUS RINGS

In a storage ring, sometimes there are advantages to work with a lattice having a smaller slippage factor η. One reason is the achievement of shorter bunch lengths. It can be shown easily that, in electron rings where the energy spread is determined by synchrotron radiation, the bunch length is proportional to $|\eta|^{1/2}$. For proton or muon storage rings where there is no synchrotron radiation, the bunch length at fixed rf voltage is proportional to $|\eta|^{1/4}$. Another reason for having a small slip factor is the possible reduction of the expensive rf system. To maintain a bunch at the required rms length σ_τ and momentum spread σ_δ, the synchrotron tune is

$$\nu_s = \frac{|\eta|\sigma_\delta}{\omega_0\sigma_\tau} \ , \tag{18.1}$$

and the rf voltage is therefore

$$V_{\rm rf} = \frac{2\pi|\eta|\beta^2 E_0\sigma_\delta^2}{eh\omega_0^2\sigma_\tau^2|\cos\phi_s|} \tag{18.2}$$

which decreases linearly as $|\eta|$. In above, h is the rf harmonic, ϕ_s is the synchronous phase angle, E_0 is the total energy of the synchronous particle which has angular revolution frequency ω_0 and velocity βc where c is the velocity of light. Ideally, when $\eta=0$, no rf will be necessary, because there will not be any drift in phase. A ring with $\eta=0$, i.e., operating right at transition energy, is called an *isochronous* ring. However, there is always a spread in energy in the beam particles. As a result, it is not possible for every beam particle to see isochronicity. In addition, the slippage factor η is a nonlinear function of the momentum spread. Usually, isochronicity is defined when the slippage factor vanishes in the first order of the momentum spread. The higher-order contributions will provide a finite slippage. Thus, the ring is actually quasi-isochronous. For such a ring, the parameters of interest are (1) η for the synchronous particle and (2) the total spread in η seen by all the beam particles. It is necessary to design the lattice so that both η and the spread in η are small. When η is vanishing small, there will not be any Landau damping and collective instabilities will emerge as an important issue, which we are going to investigate in this chapter.

18.1 Higher-Order Momentum Compaction

Transition crossing is defined as the moment when the relativistic gamma of the particle is equal to γ_t of the accelerator ring. Let us recall that the transition gamma is defined as $\gamma_t = \alpha_0^{-1/2}$, where α_0 is the momentum-compaction factor which is the fractional increment of the circumferential orbit length of a particle with fractional momentum offset δ. Hence, if $C(\delta)$ is the length of the off momentum orbit,

$$C(\delta) = C_0(1 + \alpha_0\delta) \ , \tag{18.3}$$

with $C_0 = C(0)$ being the length of the on-momentum orbit. Thus, the slippage factor η is exactly zero at transition. However, Eq. (18.3) only gives the linear dependence of the orbit length on momentum offset. In general, this is never the case for any accelerator lattice. Therefore, Eq. (18.3) should be extended to*

$$C(\delta) = C_0\big[1 + \alpha_0\delta(1 + \alpha_1\delta + \alpha_2\delta^2 + \cdots\ )\big] \ , \tag{18.4}$$

where α_1, α_2, etc. are called the high-order components of the momentum-compaction factor. Now the slippage factor η also becomes momentum spread dependent. Its higher orders must be carefully defined so that it enters correctly into Eq. (16.3), the phase-slip equation of motion

$$\frac{d\Delta\phi}{dt} = h\omega_0\eta\delta \ . \tag{18.5}$$

Here, we follow a derivation of Edwards and Syphers [1]. A particle with momentum offset δ_n sees an *accumulated* rf phase ϕ_n on its nth passage of the rf cavity, which is

*In Europe, α_0, α_1, α_2, etc. are usually referred to as α_1, α_2, α_3, etc. There is also another common definition, where $C(\delta) = C_0\big[1 + \alpha_0\delta + \alpha_1\delta^2 + \alpha_2\delta^3 + \cdots\ \big]$.

considered to have an infinitesimal length. On its $(n{+}1)$th passage, at a time $T_{n+1}+\Delta T_{n+1}$ later, the accumulated rf phase seen becomes

$$\phi_{n+1} = \phi_n + \omega_{\rm rf}(T_{n+1} + \Delta T_{n+1}) \ , \tag{18.6}$$

where $\omega_{\rm rf}/2\pi$ is the rf frequency, T_{n+1} is the revolution period of the synchronous particle during its $(n{+}1)$th turn and ΔT_{n+1} is the extra time taken by the off-momentum particle to complete the revolution. On the other hand, the rf phase seen by the synchronous particle accumulates according to

$$\phi_n^s = \omega_{\rm rf} t_n \ , \tag{18.7}$$

where t_n is the total accumulated time up to the nth passage of the cavity. Naturally, we like to measure the rf phase seen by the off-momentum particle relative to the synchronous particle. This leads to the introduction of the rf phase offset or rf phase slip $\Delta\phi_n$ defined by

$$\Delta\phi_n = \phi_n - \phi_n^s = \phi_n - \omega_{\rm rf} t_n \ . \tag{18.8}$$

Substituting into Eq. (18.6) and noting that $T_{n+1} = t_{n+1} - t_n$, we arrive at

$$\Delta\phi_{n+1} = \Delta\phi_n + \omega_{\rm rf}\Delta T_{n+1} \ . \tag{18.9}$$

In order for the synchronous particle to be synchronized, one must adjust the rf frequency so that $\omega_{\rm rf}T_{n+1} = 2\pi h$ for all turns, where h is the rf harmonic number. Now, we can define the slippage factor as the slip in revolution period at the $(n{+}1)$th passage of the cavity by

$$\frac{\Delta T_{n+1}}{T_{n+1}} = \eta_{n+1}\delta_{n+1} \ . \tag{18.10}$$

Here, the subscript of η implies its dependence on the momentum offset of the particle at the $(n{+}1)$th passage and *not* its higher-order expansion terms. With this definition, Eq. (18.9) becomes

$$\frac{\Delta\phi_{n+1} - \Delta\phi_n}{T_{n+1}} = \eta_{n+1}\omega_{\rm rf}\delta_{n+1} \ . \tag{18.11}$$

When smoothing is applied, we obtain the phase-slip equation of Eq. (16.10),

$$\frac{d\Delta\phi}{dt} = h\omega_0\eta\delta \ . \tag{18.12}$$

Since the revolution period T can be expressed as

$$T = \frac{C}{\beta c} \ , \tag{18.13}$$

we can easily expand T as a Taylor series in δ, from which each higher-order of the slippage factor can be identified. For example, we have

$$\frac{T_0'}{T_0} = \frac{C_0'}{C_0} - \frac{\beta_0'}{\beta_0} ,$$

$$\frac{T_0''}{T_0} = \frac{2{C_0'}^2}{C_0^2} - \frac{2\beta_0' C_0'}{\beta_0 C_0} - \frac{\beta_0''}{\beta_0} + \frac{2{\beta_0'}^2}{\beta_0^2} ,$$

$$\frac{T_0'''}{T_0} = \frac{C_0'''}{C_0} - \frac{3\beta_0' C_0''}{\beta_0 C_0} - \frac{3\beta_0'' C_0'}{\beta_0 C_0} + \frac{6{\beta_0'}^2 C_0'}{\beta_0^2 C_0} - \frac{\beta_0'''}{\beta_0} - \frac{\beta_0'\beta_0''}{\beta_0^2} - \frac{6{\beta_0'}^3}{\beta_0^3} , \tag{18.14}$$

where the *prime* denotes differentiation with respect to δ and all variables are evaluated at the synchronous particle, which explains why all the variables above carry the subscriptions zero, although these subscripts may have been suppressed in many occasions for the sake of convenience. The derivatives of C can be read off easily from Eq. (18.4). The derivatives of β can be computed straightforwardly. They are:

$$\frac{\beta_0'}{\beta_0} = \frac{1}{\gamma_0^2} ,$$

$$\frac{\beta_0''}{\beta_0} = -\frac{3\beta_0^2}{\gamma_0^2} ,$$

$$\frac{\beta_0'''}{\beta_0} = -\frac{3\beta_0^2(1-5\beta_0^2)}{\gamma_0^2} . \tag{18.15}$$

With the expansion of the slippage factor

$$\eta = \eta_0 + \eta_1\delta + \eta_2\delta^2 + \cdots , \tag{18.16}$$

we obtain the expressions for the higher-order components of the slippage factor [Exercise 18.1]:

$$\eta_0 = \alpha_0 - \frac{1}{\gamma_0^2} , \tag{18.17}$$

$$\eta_1 = \alpha_0\alpha_1 + \frac{3\beta_0^2}{2\gamma_0^2} - \frac{\eta_0}{\gamma_0^2} , \tag{18.18}$$

$$\eta_2 = \alpha_0\alpha_2 + \frac{\alpha_0\alpha_1}{\gamma_0^2} - \frac{2\beta_0^4}{\gamma_0^2} + \frac{3\alpha_0\beta_0^2}{2\gamma_0^2} + \frac{\eta_0}{\gamma_0^4} . \tag{18.19}$$

Looking at the phase-slip equation above, one may be tempted to equate $d\Delta\phi/dt$ to $-\Delta\omega/h$, where $\Delta\omega$ is the slip in angular velocity of the off-momentum particle relative to the synchronous particle. However, this will translate the definition of η to

$$\frac{\Delta\omega}{\omega_0} = -\eta\delta \ , \tag{18.20}$$

which is different from Eq. (18.10) and therefore will lead to incorrect expressions for the higher-order terms of η. This misconception comes about in the smoothing procedure from Eq. (18.11) to Eq. (18.12), where we divide throughout by the revolution period of the *synchronous* particle. If $\Delta\omega$ of the off-momentum particle is desired, one should divide instead by $T_{n+1} + \Delta T_{n+1}$, the revolution period of the off-momentum particle. In other words, $d\Delta\phi/dt$ in the phase equation describing the motion of an off-momentum particle does not imply the rate of change of rf phase slip of the off-momentum particle according to the clock that registers the revolution period of that particle. Instead, it is referenced to the clock that registers the revolution period of the synchronous particle. Because of this easily-forgotten detail, it will be more convenient to use $s = v_0 t$ as the independent 'time' variable, where s is the distance measured along the closed orbit of the synchronous particle and v_0 is the velocity of the synchronous particle.

Another definition in the literature is [2]

$$\eta = -\frac{1}{\omega_0}\frac{d\omega}{d\delta} \ , \tag{18.21}$$

which is incompatible with the phase-slip equation in Eq. (18.12). This definition originates from the lowest order expansion in ω [2], and is therefore insufficient when higher-orders in η are studied. This is, in fact, a variation of the incorrect definition of Eq. (18.20).

18.2 η_1-Dominated Bucket

To save the cost of rf power, suggestions have been made to make storage rings *isochronous* or *quasi-isochronous*, implying an operation when $\eta_0 \approx 0$. Since the drift of the longitudinal phase is small, a small rf system will be adequate. However, when η_0 is small enough, we need to include the next lowest nonlinear term of the slippage factor, namely η_1. When the rf phase slip $\Delta\phi$ and the fractional momentum spread δ are used as canonical coordinates with time t being the independent variable, the Hamiltonian describing

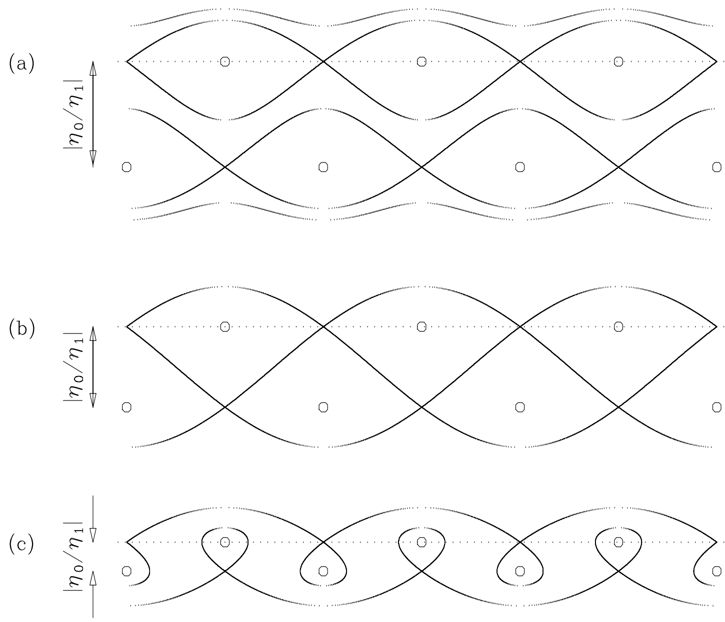

Figure 18.1: (a) When $|\eta_0/\eta_1|$ is not too small, the longitudinal phase space shows 2 series of distorted pendulum-like buckets. (b) As $|\eta_0/\eta_1|$ decreases to the critical value in Eq. (18.23), the 2 series merge. (c) Further reduction of $|\eta_0/\eta_1|$ leads to new pairing of stable and unstable fixed points and the buckets become α-like. In each case, the dotted line is the phase axis at zero momentum spread, and the small circles are the stable fixed points.

the motion of a particle in the longitudinal phase space becomes

$$H = \left(\frac{\eta_0\delta^2}{2} + \frac{\eta_1\delta^3}{3}\right) h\omega_0 + \frac{eV_{\rm rf}\omega_0}{2\pi\beta^2 E_0}\left[\cos(\phi_s+\Delta\phi) + \Delta\phi\sin\phi_s\right] , \tag{18.22}$$

where ϕ_s is the synchronous phase. With the presence of η_1, the symmetry of the higher- and lower-momentum parts of the phase space is broken. As a result, the phase-space structure will be very much disturbed. This Hamiltonian gives stable fixed points at $(2n\pi, 0)$, $(2(n+1)\pi - 2\phi_s, -\eta_0/\eta_1)$ and unstable fixed points at $(2(n+1)\pi - 2\phi_s, 0)$, $(2n\pi, -\eta_0/\eta_1)$, where n is any integer. When the contribution of η_1 is much smaller than that of η_0, the buckets are still roughly pendulum-like as shown in Fig. 18.1(a) for the case of $\phi_s = 0$. Note that there is another series of buckets at momentum spread $-\eta_0/\eta_1$. As $|\eta_0/\eta_1|$ decreases to a point when the values of the Hamiltonian through all unstable fixed points are equal, the two series merge as illustrated in Fig. 18.1(b). This happens when

$$\left|\frac{\eta_0}{\eta_1}\right| = \left\{\frac{6eV_{\rm rf}}{\pi\beta^2 h\eta_0 E_0}\left[\left(\frac{\pi}{2}-\phi_s\right)\sin\phi_s - \cos\phi_s\right]\right\}^{1/2} . \tag{18.23}$$

The right side is just $\sqrt{3}$ times the half bucket height when the η_1 term in the Hamiltonian is absent. As $|\eta_0/\eta_1|$ is further reduced, the pairing of the stable and unstable fixed points is altered, and the buckets become α-like as illustrated in Fig. 18.1(c). The buckets in one series have heights given by

$$\hat{\delta} = \begin{cases} +\left|\dfrac{\eta_0}{2\eta_1}\right| & \delta > 0 \ , \\ \\ -\left|\dfrac{\eta_0}{\eta_1}\right| & \delta < 0 \ . \end{cases} \tag{18.24}$$

For the other series, the buckets are just inverted and are centered at $\delta = -|\eta_0/\eta_1|$. Note that the heights of the buckets will vanish if the lattice approaches truly isochronous ($\eta_0 = 0$).

Let us now review some very peculiar properties of the α-like bucket.

(1) Since the height of the α-shape bucket is fixed, the bucket width ϕ is proportional to $V_{\rm rf}^{-1/2}$ and so is the bucket area $\mathcal{A}$ [3]. In fact,

$$\phi = \left(\frac{|\eta_0|^{3/2}}{|\eta_1|}\right)\left(\frac{2\pi\beta^2 hE_0}{3eV_{\rm rf}|\cos\phi_s|}\right)^{1/2} , \tag{18.25}$$

$$\mathcal{A} = \frac{6}{5}\left(\frac{|\eta_0|^{5/2}}{\eta_1^2}\right)\left(\frac{2\pi\beta^2 hE_0}{eV_{\rm rf}|\cos\phi_s|}\right)^{1/2} , \tag{18.26}$$

where the narrow width of the bucket has been assumed and its maximum momentum spreads of $|\eta_0/(2\eta_1)|$ and $-|\eta_0/\eta_1|$ have been used. Unlike the usual pendulum-like bucket where the bucket width is fixed and the bucket height and area increase with the rf voltage, here, this α-like bucket has fixed height while its width and area will be increased by *lowering* the rf voltage. As an example, set the bucket height to $|\eta_0/\eta_1| = k_\delta\delta_{\rm max}$ and the bucket half width to $\hat{\ell} = k_\ell \ell_{\rm max}$, where $\delta_{\rm max}$ and $\ell_{\rm max}$ are the maximum bunch momentum spread and length in m. The required rf voltage multiplied by the rf harmonic required to maintain the bunch in the bucket is, according to Eq. (18.25),

$$hV_{\rm rf} = \frac{2\pi\beta^2 E_0 R^2|\eta_0|k_\delta^2\delta_{\rm max}^2}{3ek_\ell^2\ell_{\rm max}^2|\cos\phi_s|} . \tag{18.27}$$

The maximum momentum spread and bunch length are also related by the Hamiltonian,

$$\frac{V_{\rm rf}}{h} = \frac{\pi\beta^2 E_0|\eta_0|\delta_{\max}^2}{2e\sin^2\frac{1}{2}\phi_{\max}}\left(1+\frac{2}{3k_\delta}\right) , \tag{18.28}$$

where we have set $\phi_s = 0$ or π. The maximum half phase spread is $\phi_{\max} = h\ell_{\max}/R$. Therefore, when the rf harmonic $h \ll 2R/\ell_{\max}$, Eqs. (18.27) and (18.28) give

$$\left(\frac{k_\delta}{k_\ell}\right)^2 = 3 + \frac{2}{k_\delta} , \tag{18.29}$$

which is universally true, independent of the bunch and lattice parameters.

(2) The asymmetry between positive and negative momentum spreads brought in by η_1 will lead to bunch length oscillations. Since the energy loss due to the resistive part of the impedance of the vacuum chamber is proportional to the bunch length, this may lead to a continuous growth of the synchrotron oscillation amplitude. This instability is called longitudinal head-tail, which had been observed in the CERN SPS [4]. The instability can become very strong here because η_0 has been made negligibly small.

(3) The synchrotron frequency as a function of oscillation amplitude can be computed easily [3]. As the oscillation amplitude increases, the synchrotron frequency inside the α-like bucket decreases much more slowly than that inside an ordinary pendulum-like bucket. However, it drops to zero very abruptly near the edge of the bucket. Thus, the α-like bucket resembles a resonance island more than the usual pendulum-like bucket. Because of the sudden drop of the synchrotron frequency near the separatrix, higher-order resonances due to small jitters or modulations of the rf phase or rf voltage overlap creating a thick stochastic layer thus further reducing the stable area inside the bucket.

(4) Although there are disadvantages of the α-like bucket, nevertheless, this bucket is intrinsically narrow in phase spread, as is depicted in Eq. (18.26). For a pendulum-like bucket, the bucket width is always equal to the rf wavelength, whereas for a α-like bucket, the bucket width is mostly much less than the rf wavelength. Moreover, for a bunch in an ordinary pendulum-like bucket, the bunch width varies as $(|\eta_0|/V_{\rm rf})^{1/4}$; thus reducing the momentum-compaction factor or increasing the rf voltage is not very efficient in reducing the width of the bunch. On the other hand, a bunch in the α-like bucket has a width proportional to $|\eta|^{3/2}/V_{\rm rf}^{1/2}$.

18.3 η_2-Dominated Bucket

The η_1 term will lead to a small bucket area and possibly longitudinal head-tail instability, thus limiting the beam dynamic when the machine is near isochronous. The δ-asymmetric bucket can lead to unpleasant longitudinal head-tail instability. Furthermore, α_1 can destroy the isochronicity of the ring. For example, if we want to have a 2 TeV on 2 TeV isochronous ring for the muon collider with $|\eta| \lesssim 1 \times 10^{-6}$, the α_1 term can contribute a a spread of γ_t^{-2} of $\sim 70 \times 10^{-6}$ at the momentum spread of $|\delta| < 0.3\%$ [5]. A large spread in γ_t^{-2} implies large slippage factors for some particles, so that an unusually large rf system will be required for bunching. Therefore, η_1 should be eliminated. Then, the Hamiltonian with the next nonlinear term η_2 included becomes

$$H = \left(\frac{\eta_0 \delta^2}{2} + \frac{\eta_2 \delta^4}{4} \right) h\omega_0 + \frac{eV_{\rm rf}\omega_0}{2\pi\beta^2 E_0} \left[\cos(\phi_s + \Delta\phi) + \Delta\phi \sin\phi_s \right] . \tag{18.30}$$

A quadrupole bends particles with positive and negative off-momenta in opposite directions. To the lowest order, it contributes to α_0 of the momentum-compaction factor. On the other hand, a sextupole bends particles with positive and negative off-momenta in the same direction, and therefore contributes to α_1. In fact, through first-order perturbation theory, one can show that α_2 can be corrected with octupoles, α_3 with decapoles, and so on [6, 7]. Having the ability to change α_2 with octupoles may be useful because it may be easier than adjusting α_2 with sextupoles since the latter also affect α_1.

With the contribution of η_1 eliminated, it is possible to adjust η_0 to zero so that the Hamiltonian becomes

$$H = \frac{1}{4} h\omega_0 \eta_2 \delta^4 + \frac{eV_{\rm rf}\omega_0}{2\pi\beta^2 E_0} \left[\cos(\phi_s + \Delta\phi) + \Delta\phi \sin\phi_s \right] , \tag{18.31}$$

Now for $\phi_s = 0$, the bucket looks pendulum-like with the usual width of $\Delta\phi = 2\pi$. The bucket half height is $\hat{\delta} = [4eV_{\rm rf}/(\pi\beta^2 E_0 h|\eta_2|)]^{1/4}$. When the half bunch length $\ell_{\rm max}$ is short, it is related to the half momentum spread $\delta_{\rm max}$ by

$$\delta_{\rm max}^4 = \left(\frac{eV_{\rm rf} h}{\pi\beta^2 E_0 |\eta_2|} \right) \left(\frac{\ell_{\rm max}}{R} \right)^2 . \tag{18.32}$$

If we let $\hat{\delta} = k\delta_{\rm max}$, we can solve for the necessary rf voltage and rf harmonic:

$$V_{\rm rf} = \frac{\pi\beta^2 E_0 R k^2 \Delta\eta \delta_{\rm max}^2}{2\ell_{\rm max}} , \quad h = \frac{2R}{\ell_{\rm max} k^2} , \tag{18.33}$$

where $\Delta\eta = |\eta_2|\delta_{\rm max}^2$ is the desired spread of the slippage factor of the bunch. Note that the rf voltage is proportional to $\Delta\eta$, the desired spread in momentum-compaction, and $\delta_{\rm max}^2$, the momentum spread of the bunch squared. Thus, if we reduce the momentum-compaction spread, the rf voltage will be reduced by the same factor. On the other hand, the rf frequency is independent of the choice of $\Delta\eta$ and $\delta_{\rm max}$.

For small phase spread, Eq. (18.31) describes a particle oscillating in a quartic potential (with $\Delta\phi$ and δ interchanged). This is a well-known situation when a higher harmonic cavity is present and the two cavity voltages are inversely proportional to the square of their respective harmonics (see Sec. 9.3.1). For such a system, the synchrotron frequency is zero at zero oscillating amplitude and increases linearly with respect to the momentum offset $\delta_{\rm max}$, or the 4th root of the Hamiltonian. The synchrotron frequency increases to a maximum for larger oscillation amplitude and drops to zero again at the edge of the bucket. Simple derivation gives the synchrotron tune $\nu_s = \nu_{s0}F(H)$, where $\nu_{s0} = \sqrt{h\Delta\eta eV_{\rm rf}/(2\pi\beta^2E_0)}$ with $\Delta\eta = |\eta_2|\delta_{\rm max}^2$ just the synchrotron tune of a synchronous particle in an ordinary single rf system with a slippage factor equal to $\Delta\eta$. For a constant η_2, the ν_{s0} is directly proportional to the momentum-offset excursion $\delta_{\rm max}$. The form factor $F(H)$ can be written as (Exercise 18.5)

$$F^{-1}(H) = \frac{2^{3/4}}{2\pi}\int_0^{\pi/2}\frac{dz}{\sqrt{\cos z}\sqrt{1-\sin^2\frac{\phi_{\rm max}}{2}\sin^2 z}}\ . \tag{18.34}$$

The form factor is evaluated at the Hamiltonian value,

$$H = \frac{eV_{\rm rf}\omega_0}{\pi\beta^2E_0}\sin^2\frac{\phi_{\rm max}}{2} = \tfrac{1}{4}h|\eta_2|\omega_0\delta_{\rm max}^4\ , \tag{18.35}$$

where $\phi_{\rm max}$ and $\delta_{\rm max}$ are equal to, respectively, the phase and momentum-offset excursions of the beam particle under investigation. A large spread in synchrotron frequency can be advantageous in providing Landau damping to mode-coupling instabilities. For small $\phi_{\rm max}$, from Eqs. (18.33) and (18.35), one obtains $\sin^2(\phi_{\rm max}/2) = k^{-4}$, where $k = \hat{\delta}/\delta_{\rm max}$. Thus, the form factor of Eq. (18.34) is almost a constant for any reasonable k, and is roughly equal to $F(H) = 1.45$.

18.4 Microwave Instability Near Transition

18.4.1 Analytic Solutions

In an operation near the transition energy ($\eta_0 \approx 0$), at least the next order, η_1 in Eq. (18.16), must be included for a meaningful discussion of the beam dynamics. Bogacz analyzed the stability of a coasting beam right at transition, $\eta_0 = 0$ [8], by including the η_1 term but neglecting other higher-order terms. For a Gaussian distribution with rms energy spread σ_E, he obtained an analytic expression for the growth rate at the revolution harmonic n:

$$\frac{1}{\tau_n} = -2\alpha_1 n\omega_0 \left(\frac{\sigma_E}{E_0}\right)^2 \phi_n \qquad \text{with} \qquad \tan\phi_n = \left[\frac{\mathcal{I}m\, Z_0^{\parallel}}{\mathcal{R}e\, Z_0^{\parallel}}\right]_n , \tag{18.36}$$

where $\mathcal{I}m\, Z_0^{\parallel} > 0$ implies capacitive and $\omega_0/(2\pi)$ is the revolution frequency of the on-energy particle which has energy E_0. He drew the conclusion that the beam will be completely stable. However, when he made this conclusion, he had in mind the assumption of $\alpha_1 > 0$ and $\phi_n > 0$, which is not always true. As a result, there will be microwave growth in general.

Holt and Colestock studied the same problem with coasting beam and Gaussian energy distribution, but allowing $\eta_0 \neq 0$ [9]. The dispersion relation is expressed in terms of the complex error function. Their conclusion is that there is no unstable region in the complex $Z_0^{\parallel}$-plane below transition. On the other hand, there are both stable and unstable regions above transition. They also claimed that their conclusion was supported by simulations. However, they did not specify the values of η_0 and η_1 in the simulations they presented or in their stability plots in the complex $Z_0^{\parallel}$-plane. It is hard to understand at least the situation below transition. It is clear that when $|\eta_0|$ is not too small, the contribution of η_1 is irrelevant. Thus their claim as stated can be interpreted as *no microwave instability below transition*, no matter how far away it is from transition. For this reason, this claim is quite questionable. When we look into the stability plots of Holt and Colestock, Fig. 18.2, we can see something that resembles a stability curve below transition. The presence of a stability curve implies the existence of both stable and unstable regions, in contradiction to their conclusion.

We performed some simulations and got different results. A coasting beam at 100 GeV was considered in a hypothetical ring of circumference 50 m, with an initial rms

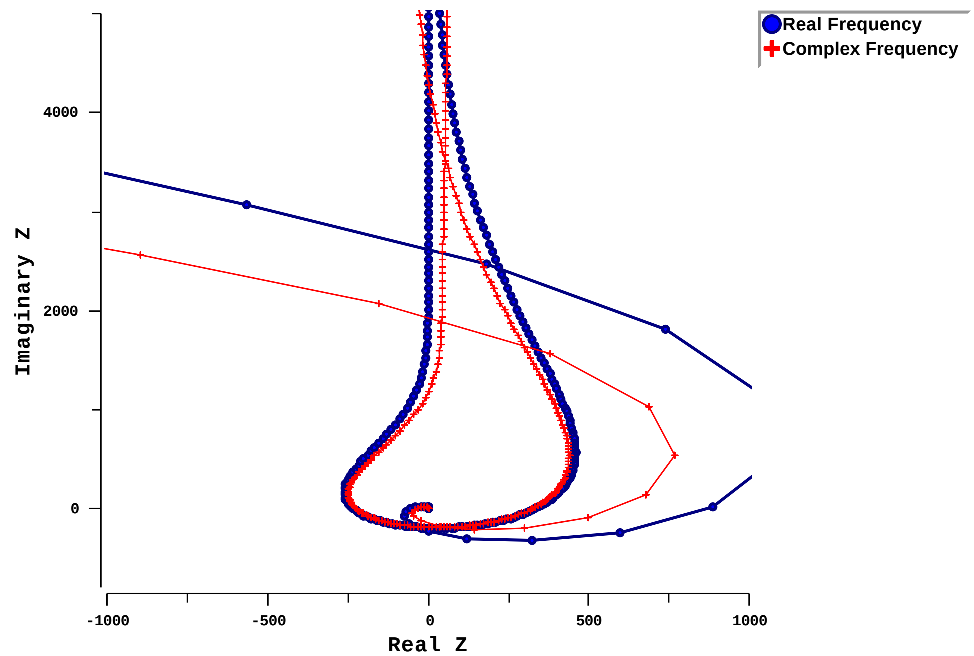

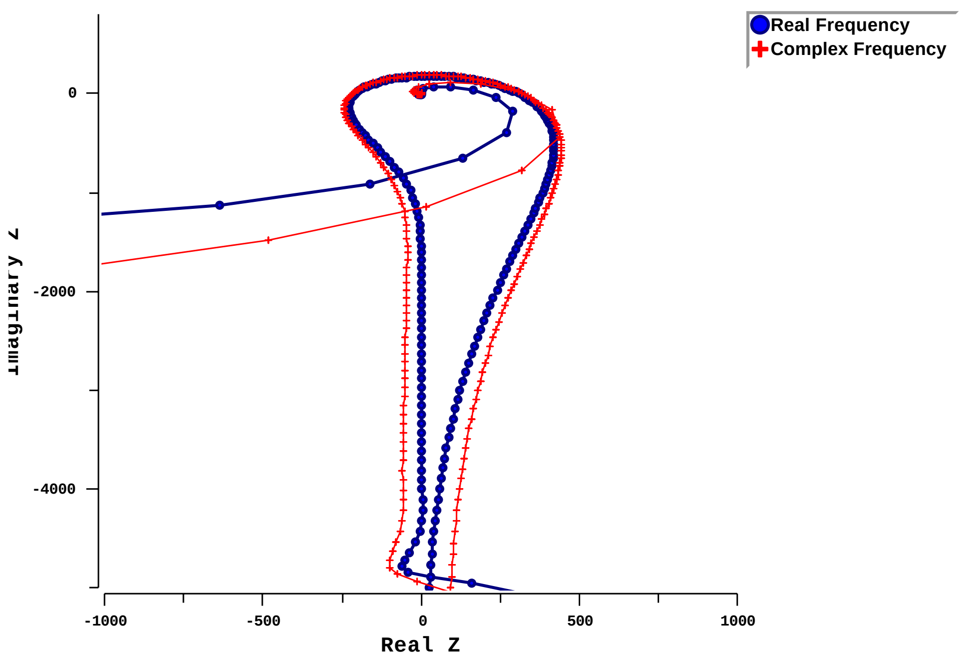

Figure 18.2: (color) Dispersion relation plots in the complex impedance plane. The thick blue curves with circles are for real frequencies and therefore should exhibit the stability boundaries. The red curves with +'s are for complex frequencies. Top plot is below transition and bottom plot is above transition.

parabolic fractional momentum spread of 0.001, interacting with a broadband impedance of $Z_0^{\parallel}/n = 3.00\ \Omega$ at the resonance frequency of 600 MHz and quality factor $Q = 1$. This unrealistic small size of ring was chosen because we wanted to limit the number of longitudinal bins around the ring so that not so many macro-particles would be necessary. In the tracking, the bin size had been chosen to be 0.25 m, which was half the wavelength at 600 MHz. With the slip factor fixed at $|\eta| = 0.005$, the beam intensity was adjusted so that the Keil-Schnell circle-approximated criterion [10] gave a stability limit of $|Z_0^{\parallel}/n| = 1.00\ \Omega$. All higher-order slip factors were set at zero. The tracking results are shown in Fig. 18.3: the top 4 plots for $\eta = -0.005$ (below transition) and the lower 4 plots for $\eta = +0.005$ (above transition) at 0, 1200, 2400, and 3600 turns. We see that below transition irregularities develop at the low-momentum edge. Ripples corresponding to the frequency of 600 MHz (wavelength = 0.5 m) are clearly seen. The momentum spread broadens at the low-momentum side until the total spread is about 1100 MeV, about 2.75 times the original total spread of about 400 MeV. This is partly because of the energy loss as a result of the resistive part of the impedance. The observation definitely confirms the occurrence of microwave instability below transition, and the eventual self-stabilization by overshooting. Above transition, irregularities also develop at the low-momentum edge and the momentum spread also broadens at the low-momentum edge. The total spread appears to be broader than the situation below transition. In addition, we see small bomb-like droplets launched at the low-momentum side, which are not observed below transition. Instability above transition appears to be more severe than below transition. We will come back to the simulations of coasting beam near transition later in Sec. 18.4.3.

18.4.2 Bunched Beam Simulations

In this section, we study the stability of a bunched beam very close to transition. As an example, take a muon bunch in the proposed 50×50 GeV muon collider, which has a slip factor of $|\eta| = 1 \times 10^{-6}$. Everything we discuss here will apply to a proton bunch also, with the exception that the muons decay while the protons are stable. We will first discuss the situation with the decay of the muons taken into consideration, and later push the lifetime to infinity. We assume that sextupoles and octupoles are installed and adjusted so that the contributions of η_1 and η_2 become insignificant compared with η_0. The muon bunch we consider has an intensity of $N_b = 4 \times 10^{12}$ particles, rms width $\sigma_\ell = 13$ cm and rms fractional momentum spread $\sigma_\delta = 3 \times 10^{-5}$ or $\sigma_E = 1.5$ MeV.

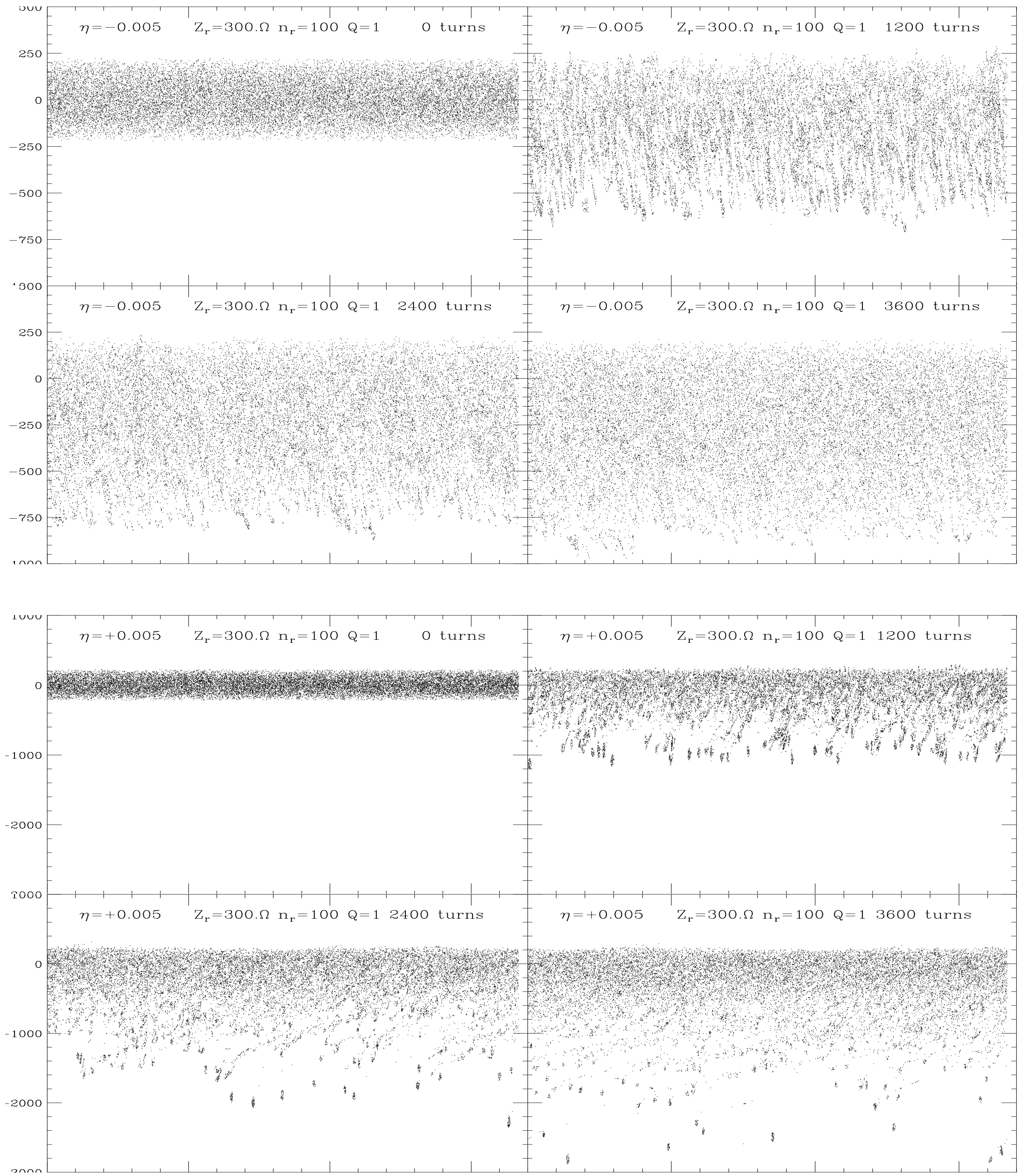

Figure 18.3: The top 4 plots and lower 4 plots are for $\eta = -0.005$ (below transition) and $\eta = +0.005$ (above transition), respectively, at 0, 12000, 24000, and 36000 turns. The impedance is a broadband with $Q = 1$, $Z_0^{\|}/n = 3.0\ \Omega$ at the resonant frequency of 600 MHz.

The impedance is assumed to be broadband with $Z_0^\parallel/n = 0.5\ \Omega$ at the angular resonant frequency of $\omega_r = 50$ GHz with quality factor $Q = 1$. The muons have an e-folding lifetime of 891 turns at 50 GeV in this collider ring. During the muon lifetime, there is negligible phase motion. Thus a bunching rf frequency system is not necessary. However, as will be explained below, rf systems are needed for the cancellation of potential-well distortion.

For bunched beams, there is the issue of potential-well distortion which must not be mixed up with the collective microwave instability. Potential-well distortion will change the shape of the bunch to something that looks like the plot of Fig. 18.4, with the difference that the distortion of the beam does not come from the space charge force, but mainly from the inductive part of the broadband impedance.

The wake potential seen by a particle inside a Gaussian bunch at a distance z behind the bunch center is shown in Fig. 18.5 and is given by

$$V(z)=e\int_{-\infty}^{z} dz'\rho(z')W_0(z-z')=-\frac{eN\omega_r R_\parallel}{2Q\cos\phi_0}\,\mathcal{R}e\, e^{i\phi_0-z^2/(2\sigma_\ell^2)}w\left[\frac{\sigma_\ell\omega_r e^{i\phi_0}}{c\sqrt{2}}-\frac{iz}{\sqrt{2}\sigma_\ell}\right], \tag{18.37}$$

where $\rho(z)$ is the bunch distribution, $W_0(z)$ the longitudinal wake function, $\sin\phi_0 = 1/(2Q)$, and w is the complex error function. This distortion can be cancelled up to $\pm 3\sigma_\ell$ by 2 rf systems [11], which at injection are at frequencies $\omega_1/(2\pi) = 0.3854$ GHz and $\omega_2/(2\pi) = 0.7966$ GHz, with voltages $V_1 = 65.40$ kV and $V_2 = 24.74$ kV, and phases $\varphi_1 = 177.20^\circ$ and $\varphi_2 = 174.28^\circ$. This compensation is shown in Fig. 18.5. Since only 2 sinusoidal rf's are used, the cancellation is not complete; however, the error is less than 1% of the original wake potential and is considered to be not important. Because of the lifetime of the muons, we first performed tracking for only 1000 turns in the time domain using the broadband wake function $W_0(z)$. The initial and final bunch distributions are shown in Fig. 18.6. During the simulation the compensating rf voltages were lowered turn by turn to conform with the diminishing bunch intensity due to the decay of the muons.

We see from the right plot of Fig. 18.6 that the bunch distribution has been very much distorted after 1000 turns. This comes mostly from the fact that the original distribution of the bunch in the left plot is not exactly Gaussian. It consists of 2×10^6 macro-particles randomly distributed according to a bi-Gaussian distribution. As a result, the wake potential of the actual bunch shown as a red dotted curve in Fig. 18.7 deviates slightly from and wiggles around the ideal wake potential curve of a smooth

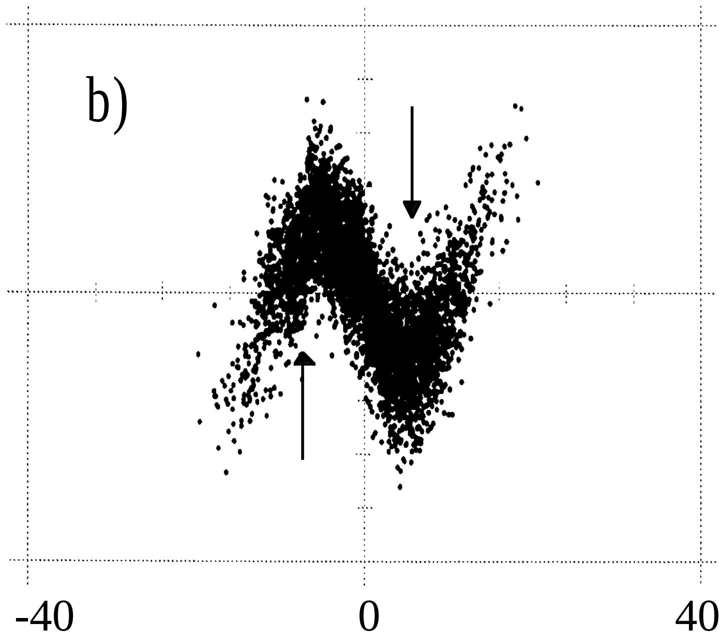

Figure 18.4: Effects of a strong space charge or potential-well distortion force result in a N-shape vertical shear on the bunch.

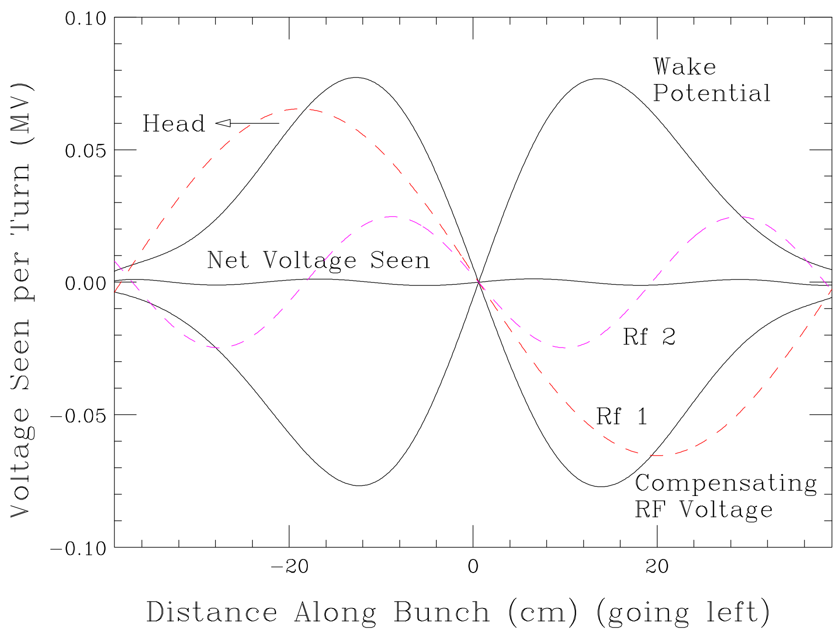

Figure 18.5: (color) Wake potential, compensating rf voltages, and net voltage seen by particles in the 13-cm bunch at injection. The compensating rf is the sum of two rf's represented by dashes.

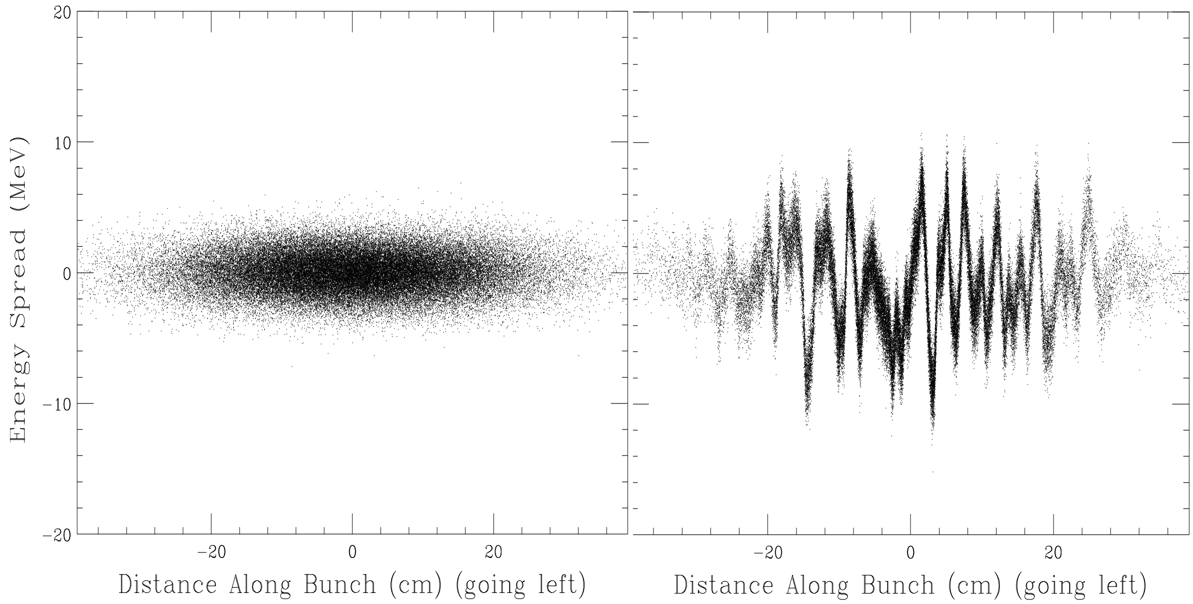

Figure 18.6: Simulation of the 13-cm bunch of 4×10^{12} muons subject to a broad-band impedance with quality factor $Q = 1$ and $Z_{\|}/n = 0.5\ \Omega$ at the resonant angular frequency $\omega_r = 50$ GHz. The half-triangular bin width is 15 ps (0.45 cm) and 2×10^6 macro-particles are used. Left plot shows initial distribution with $\sigma_E = 1.5$ MeV and $\sigma_\ell = 13$ cm. Right plot shows distribution after 1000 turns with compensating rf's depicted in Fig. 18.5.

Gaussian bunch shown in solid. The difference is the magenta dotted jitter curve in the center of the plot. The fluctuation seen in the right plot of Fig. 18.6 is the result of the accumulation of this dotted jitter curve in 1000 turns with muon decay taken into account. Although this tiny fluctuation leads to a small potential-well distortion in one turn ($\leq$ 0.02 MeV), it is unfortunate that this distortion accumulates turn after turn and will never reach a steady state, since the beam is so close to transition[†]. (For an electron bunch, this growth will stop when it is balanced by radiation damping.) This accumulated distortion can be computed exactly from the the dotted jitter curve. Any growth in excess will come from collective microwave instability. Note that the uncompensated potential-well distortion is quite different from the growth due to microwave instability. For the former, the growth in energy fluctuations every turn will be exactly

[†]More exactly, a steady state will be reached when the momentum offset becomes so large that phase drift due to the small slip factor becomes significant. However, this will not happen in reality because of the finite momentum aperture of the storage ring.

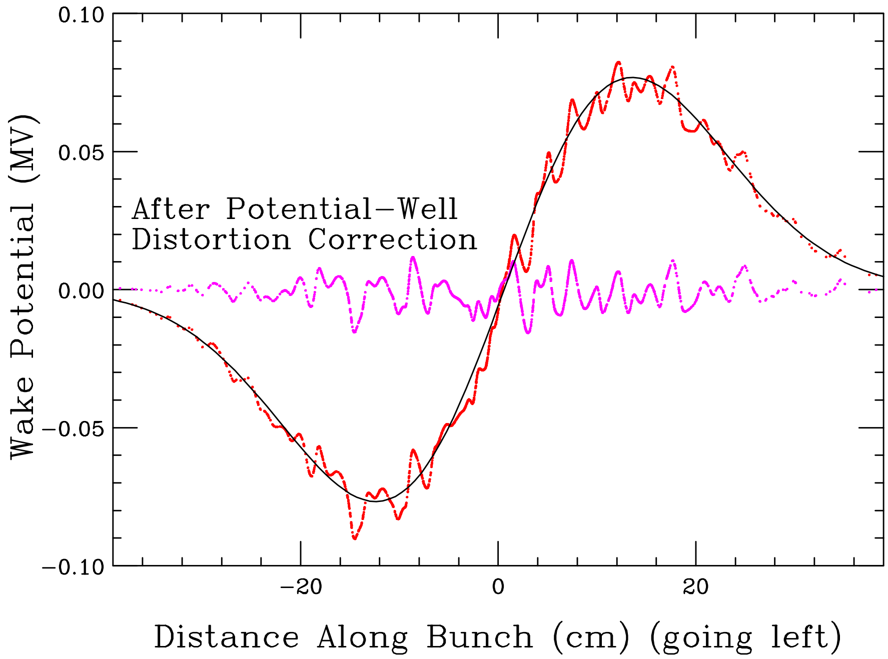

Figure 18.7: (color) Wake potential seen by the simulated bunch shown as red dots is interlaced with the wake potential of an ideal smooth Gaussian bunch shown in solid. The difference (center magenta curve) represents the random fluctuation of the finite number of macro-particles.

by the *same* amount as given by the dotted jitter curve in Fig. 18.7 (if muon decay is neglected). This is because the wake potential of particles along the bunch does not depend on the energy distribution of the bunch, but only on its linear density and the latter is essentially unchanged since the particles do not drift much during the first 1000 turns. On the other hand, the initial growth due to microwave instability at a particular turn is proportional to the actual energy fluctuation at that turn and the evolution of the growth is exponential. Thus, although the growth due to microwave instability is small at the beginning, it will be much faster later on when the accumulated energy fluctuations become larger. It is worth mentioning that even if the wake potential of the initial bunch with statistical fluctuations has been compensated exactly by the rf's, the bunch can still be unstable against microwave instability. An infinitesimal deviation from the bunch distribution can excite the collective modes of instability corresponding to some eigenfrequencies. In other words, the accumulated growth due to potential-well distortion is a static solution and this static solution converges very slowly close to transition until the momentum spread is large enough for the small $|\eta|$ to smooth the distribution. Microwave instability, on the other hand, is a time dependent solution.

In Fig. 18.8, the 3 plots on the left are for a 4000-turn simulation of the same muon bunch using 2×10^6 macro-particles with the decay of the muons considered. The two compensating rf systems are turned on. The first plot is for $\eta = 0$ so that microwave instability cannot develop. All the fluctuations are due to the residual potential-well distortion or the accumulation of the uncompensated jitters. The second and third plots are for, respectively, $\eta = -1 \times 10^{-6}$ (below transition) and $\eta = +1 \times 10^{-6}$ (above transition). We see that they deviate from the first plot, showing that there are growths due to microwave instability although the effect is small. The 3 plots on the right are the same as on the left with the exception that the muons are considered stable, or, in other words, the particles can be protons. We see that the second and third plots differ from the first one by very much (note the change in energy scale), indicating that microwave instability does play an important role for proton bunches in a quasi-isochronous ring. We also see that microwave instability is more severe above transition than below transition even when the beam is so close to transition. In the simulations, the jitters, or the statistical fluctuation around the smooth distribution might have been very much exaggerated because of the small number of macro-particles included in the tracking. In a realistic beam, these statistical fluctuations should be very much smaller. However, these jitters can also come from other sources, such as electronic noises, rf acceleration, rf maneuvering, etc. These jitters will be very much larger than the Schottky noise. As a result, in the design of a quasi-isochronous ring, the sources of all jitters should be carefully considered in order to estimate the growth in energy offset due to potential-well distortion or microwave instability.

18.4.3 Coasting Beam Simulations

For coasting beams, we do not have the inverted tilted "N"-shape wake potential as in Fig. 18.5. Thus, no rf compensation will be required. However, the noise in the beam does result in a wake potential similar to the small residual wake-potential jitters in Fig. 18.5 after wake-potential compensation. Near transition where the phase motion is negligibly slow, these jitters will add up turn after turn without limit exactly in the same way as the bunched beam after having optimized the rf compensation. Thus, near transition, there is essentially no difference between a coasting beam and a bunched beam after the rf compensation. The only exception is that microwave instability develops

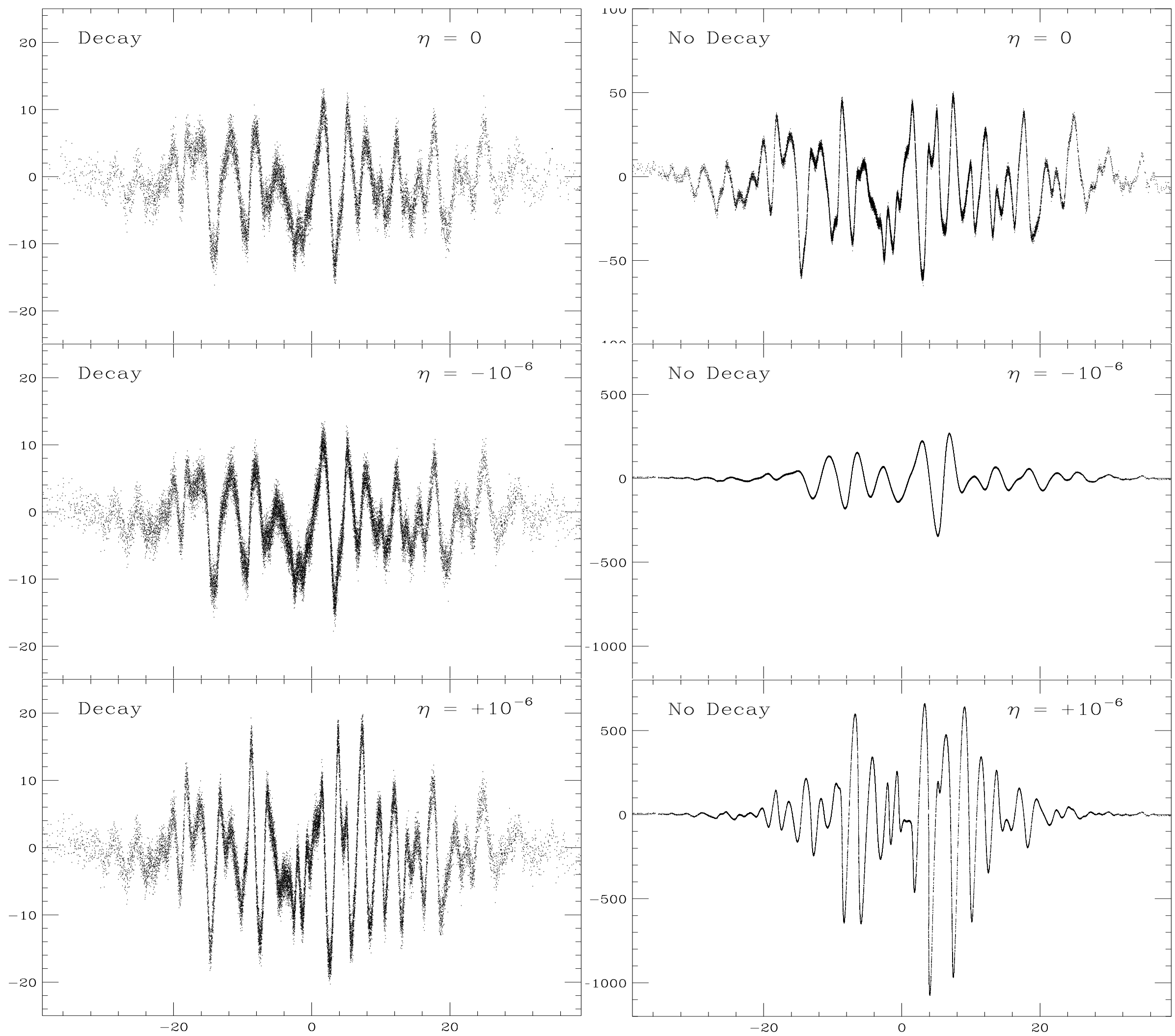

Figure 18.8: Phase-space plots of energy spread in MeV versus distance from bunch center in cm at the end of 4000 turns. All are simulating 4×10^{12} micro-particles with 2×10^{6} macro-particles. In the left 3 plots, the decay of the muons has been taken into account. The first left plot is for $\eta = 0$ so that it just gives the amount of potential-well distortion. The second and third plots are for, respectively, $\eta = -1 \times 10^{-6}$ and $+1 \times 10^{-6}$. The small deviations from the first plot are results of microwave instability. The right 3 plots are the same as the left, except that the muons are considered stable. Here, large microwave growths develop (note the change of energy scale).

most rapidly near the center of the bunch where the local intensity is highest, whereas in a coasting beam, microwave instability develops with equal probability along the bunch depending on the statistical fluctuations in the macro-particles.

In Fig. 18.9, we show some coasting beam simulations near transition by having $\eta_0 = 0$ or $\pm 5 \times 10^{-5}$ and $\eta_1 = 0$ or ± 0.05. The coasting beam consists of 3.27×10^{15} protons (or nondecaying muons) having an average energy of 100 GeV in a hypothetic ring with circumference 50 m. The initial momentum spread is Gaussian with rms fractional spread $\sigma_\delta = 0.001$ or $\sigma_E = 100$ MeV. Thus, at 1σ, the contribution of $|\eta_1| = 0.05$ is the same as the contribution of $|\eta_0| = 5 \times 10^{-5}$. The simulations are performed with 8×10^5 macro-particles in 400 triangular bins. The impedance is a broadband with $Q = 1$ and $Z_0^\parallel/n = 2\ \Omega$ at the resonant frequency of $f_r = 300$ MHz.

All the plots in Fig 18.9 are illustrated with the same scale for easy comparison. The horizontal axes are longitudinal beam position from 0 to 166.7 ns, while the vertical axes are energy spread from -4000 to 3000 MeV. Plot (a) shows the initial particle distribution in the longitudinal phase space. All the other plots are simulation results at the end of 54,000 turns. Plot (b) is the result of having $\eta_0 = 0$ and $\eta_1 = 0$. It shows the accumulation of the wake-potential jitters over 54,000 turns. These jitters originate from the statistical fluctuation of the initial population of the macro-particles. Therefore, any deviation from Plot (b) implies microwave instability. Plots (c) and (d) are with $\eta_0 = 0$, but with $\eta_1 = +0.05$ and -0.05, respectively. We see the growths curl towards opposite phase directions nonlinearly as expected. This is due to the nonlinearity in δ of the time slip given by Eq. (18.16), similar to the simulations in Fig. 18.4(a). It appears that Plot (c) with $\eta_1 = -0.05$ gives a larger growth. Plots (e), (g), and (i) are for $\eta_0 = -5 \times 10^{-5}$ (below transition), but with $\eta_1 = +0.05$, -0.05, and 0, respectively. We see that the microwave instability is most severe when $\eta_1 = 0$, indicating that η_1 has the ability to curb instability. This is, in fact, easy to understand. The phase drift driven by $|\eta_1| = 0.05$ is much faster than that driven by $|\eta_0| = 5.0 \times 10^{-5}$ at larger momentum spread; for example, it will be 4 times faster at $2\sigma_\delta$, 9 times faster at $3\sigma_\delta$, etc. As a result, a nonvanishing $|\eta_1|$ tends to move particles away from the clumps, thus lessening the growth due to microwave instability.

Plots (f), (h), and (j) are for $\eta_0 = +5 \times 10^{-5}$ (above transition), but with $\eta_1 = +0.05$, -0.05, and 0, respectively. Again microwave instability is most severe when $\eta_1 = 0$, and η_1 does curb instability to a certain extent. Comparing Plots (e), (g), and (i) with Plots (f), (h), and (j), it is evident that the beam is more unstable against microwave

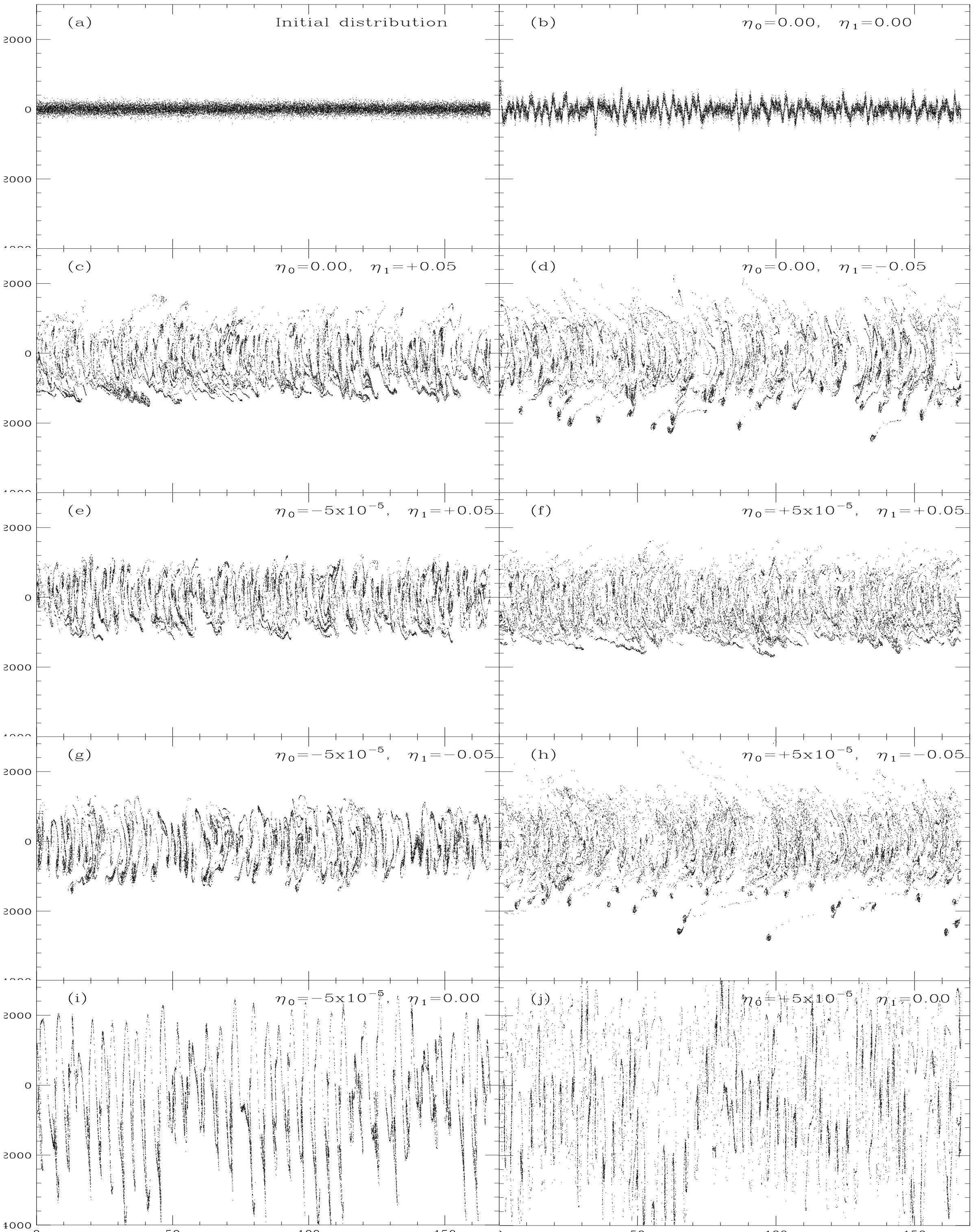

Figure 18.9: Energy spread (MeV) versus bunch position (ns) of coasting beam simulations. See text for explanation.

instability above transition ($\eta_0 > 0$) than below transition ($\eta_0 < 0$) independent of the sign of η_1. For a fixed η_0, we also notice that negative η_1 is more unstable than positive η_1. The theoretical implications of these results are nontrivial and will be discussed in a future publication.

Now let us come back to the analytic investigations by Bogacz, Holt, and Colestock. Their results appear to contradict the simulations presented here. Analytic analysis often starts with the Vlasov equation. The time-dependent beam distribution $\psi(\phi, \Delta E; t)$ can be separated into two parts:

$$\psi(\phi, \Delta E; t) = \psi_0(\phi, \Delta E) + \psi_1(\phi, \Delta E)\, e^{-i\Omega t} \ . \tag{18.38}$$

Here, ψ_0 is the *steady-state* solution of the Hamiltonian and ψ_1 describes the collective motion of the beam with the collective frequency $\Omega/(2\pi)$. After linearization, the Vlasov equation becomes an eigenequation with ψ_1 as the eigenfunction and $\Omega/(2\pi)$ the eigenfrequency. The equation also depends on ψ_0. Thus we must solve for the *steady-state* solution first before solving the eigenequation. The steady-state solution is the time-independent solution of the Hamiltonian which includes the contribution of the wake function. In other words, ψ_0 is the potential-well-distorted solution. Far away from transition, this distortion is mostly in the ϕ coordinate, for example, that brought about by the space charge or inductive forces. Therefore, for a coasting beam, there will not be any potential-well distortion at all. The situation, however, is quite different close to transition. As was pointed out in above, the potential-well distortion is now in the ΔE coordinate. For this reason, not only bunched beams, even coasting beams will suffer from potential-well distortion as a result of the nonuniformity of the beam. In simulations, the nonuniformity arrives from the statistical fluctuation of the distribution of the macro-particles. This nonuniformity will accumulate turn by turn until the momentum spread is so large that the small $|\eta|$ is able to smooth out all nonuniformity. In other words, the steady-state distribution ψ_0 that goes into the Vlasov equation will be completely different from the original distribution in the absence of the wake. In the analysis of Bogacz, Holt, and Colestock, the ideal smooth Gaussian distribution in energy was substituted for ψ_0 in the Vlasov equation. However, this is a very unstable static distribution; even a small perturbation will accumulate turn by turn with extremely slow convergence. For this reason, it is hard to understand what their results really represent.

18.5 Exercises

18.1. (1) Derive Eqs. (18.14) and (18.15), the expansions of the revolution period T and velocity β as powers of the momentum offset δ.

(2) Derive Eq. (18.20), the expansion of the slippage factor.

18.2. Figure 18.1 indicates that there are two series of pendulum-like longitudinal buckets unless it is very close to the transition energy. Explain why we see only one series under most condition. Use the Fermilab Main Injector as an example. The Main Injector has a $\gamma_t = 21.8$ (20.45 GeV) and $\alpha_1 = 0.50$. Compute the distance between the two series of buckets in fractional momentum spread when it is in a coasting mode at the injection energy of 8 GeV and at 18.5 GeV.

18.3. For a proton storage ring with $\gamma_t = 21.8$ and $\alpha_1 = 0.50$. The rf voltage is 2.5 MV and the synchrotron phase is 0°. Compute the energy at which the two series of longitudinal buckets merge.

18.4. Keeping up to η_1, for the α-like bucket,

(1) derive the relation between width and height of the bucket [Eq. (18.25)],

(2) derive the bucket area [Eq. (18.27)],

(3) derive Eq. (18.29), the universal relation between width and height of a bunch fit to the bucket.

18.5. Derive the synchrotron tune of a η_2-dominated bucket starting from the Hamiltonian of Eq. (18.31).

Answer: $\nu_s = \nu_{s0} F$, where F is given by Eq. (18.34)

Bibliography

[1] D.A. Edwards and M.J. Syphers, *An Introduction to the Physics of High Energy Accelerators*, Wiley and Sons, 1993.

[2] See for example, E.D. Courant, R. Ruth, W. Weng, L. Michelotti, D. Neuffer, and L. Teng, AIP Conf. Proc. No. 87, 36 (1982).

[3] A. Riabko, M. Bai, B. Brabson, C.M. Chu, X. Kang, D. Jeon, S.Y. Lee, and X. Zhao, Phys. Rev. **E54**, 815 (1996).

[4] D. Boussard and T. Linnecar, Proc. 2nd European Particle Accelerator Conference, Nice, June 990, Ed. P. Martin and P. Mandrillon, p. 1560.

[5] K.Y. Ng, Nucl. Instrum. Method **A404**, 199 (1998).

[6] D. Robin, H. Hama, and A. Nadji, *Experimental Results on Low Alpha Electron-Storage Rings*, Proc. Micro Bunches Workshop, Upton, NY, Sep. 28-30, 1995, Ed. E.B. Blum, M. Dienes, and J.B. Murphy, (AIP Conf. Proc. 367), p. 150; D. Robin, R. Alvis, A. Jackson, R. Holtzapple, and B. Podobedov, *Low Alpha Experiments at the ALS*, *ibib* p. 181.

[7] H. Hama, S. Takano, and G. Isoyama, Nucl. Inst. Meth. **A329**, 29 (1993).

[8] A.S. Bogacz, *Microwave Instability at Transition—Stability Diagram Approach*, *Proceedings of IEEE Particle Accelerator Conference*, p.1815 (San Francisco, CA, 1991).

[9] J.A. Holt, and P.I. Colestock, *Microwave Instability at Transition*, *Proceedings of IEEE Particle Accelerator Conference*, p.3067 (Dallas, TX, 1995).

[10] E. Keil and W. Schnell, CERN Report TH-RF/69-48, 1969.

[11] E.-S. Kim, A.M. Sessler, and J.S. Wurtele, *Phys. Rev. ST Accel. Beams*, **2**, 051001 (1999).

[12] K.Y. Ng, *Phys. Rev. ST Accel. Beams*, **2**, 091001 (1999).